nature biomedical engineering

Article

https://doi.org/10.1038/s41551-026-01660-4

Whole cross-sectional human ultrasound tomography

Received: 9 July 2024

Accepted: 17 March 2026

Published online: 24 April 2026

Check for updates

David C. Garrett[1,3], Jinhua Xu[1,3], Donghyeon Oh[1,3], Yousuf Aborahama[1], Geng Ku[1], Konstantin Maslov[1], William W. Tseng[2] & Lihong V. Wang[1]

Ultrasonography is a vital component of modern clinical care, with handheld probes routinely used for diagnostic imaging and procedural guidance. However, handheld ultrasound imaging is limited by factors such as the partial cross-sectional field of view, operator dependency, contact-induced distortion and lack of transmission contrast. Here we demonstrate a new system that enables whole cross-sectional ultrasound tomography of humans in both reflection and transmission modes. We generate two-dimensional images of the entire in vivo human cross-section in the abdomen and thighs with uniform in-plane resolution using a custom 512-element circular ultrasound receiver array and a rotating transmitter. Sequential scans with our system show strong agreement with clinical magnetic resonance imaging counterparts. To address unmet clinical needs, we explore two key applications. First, we observe abdominal adipose distributions in our images, enabling adipose thickness assessment without ionising radiation or mechanical deformation. Second, we demonstrate an approach for video-rate biopsy needle localization with respect to internal tissue features. These capabilities make whole cross-sectional ultrasound tomography a potential practical tool for clinical needs currently unmet by other modalities.

Since its inception in the mid-twentieth century, ultrasound imaging has revolutionized healthcare by enabling non-invasive and affordable visualisation of soft tissue structure and function. Early systems employed single transducers scanned linearly or circularly with participants immersed in a water bath[1,2], later followed by membranes or articulating arms to image regions in the abdomen[3,4]. Initial results were promising for disease diagnosis[5], but imaging required mechanical scanning over ~1 h (ref. 6). Later developments in transducers and electronics led to linear probes[7], where multiple channels could be used in parallel. These advances enabled the modern handheld probe, which has become the predominant form of ultrasonography across many clinical applications. However, probes require trained operation[8], have limited ability to visualize features behind bone or air pockets and provide only reflection-mode images over a narrow field of view (FOV). The FOV can be expanded by scanning the probe around the periphery of regions such as the human thigh and coregistering adjacent frames[9,10]. However, existing approaches require manual probe movement to maintain contact with the skin, which can lead to image variation between operators and systems[11,12].

More recently, alternate approaches using smaller immersion tanks with planar[13], linear[14], ring[15] or hemispherical[16] transducer arrays have been investigated for ultrasound tomography (UST) imaging of the breast[17] or limbs. These systems record both reflected and transmitted signals, enabling the generation of reflectivity, speed of sound and attenuation coefficient profiles. The extension to human-scale imaging has been historically constrained by acoustic propagation barriers, particularly at bone and air interfaces, where extreme impedance mismatches obstruct wave transmission. Nevertheless, a recent

[1]Caltech Optical Imaging Laboratory, Andrew and Peggy Cherng Department of Medical Engineering, Department of Electrical Engineering, California Institute of Technology, Pasadena, CA, USA. [2]Division of Surgical Oncology, Department of Surgery, City of Hope National Medical Center, Duarte, CA, USA. [3]These authors contributed equally: David C. Garrett, Jinhua Xu, Donghyeon Oh. e-mail: lvw@caltech.edu

study achieved whole cross-sectional imaging of ~12-cm-diameter piglets postmortem despite the presence of bone and air[18]. Although this method produces high-quality images, it requires substantial data acquisition time (15–25 min) and reconstruction time (20–25 min). Such extended protocols are challenging to adapt to in vivo human imaging owing to participant motion. These times also rival those of magnetic resonance imaging (MRI), which may limit the practicality and scalability of the technique in clinical settings. Another recent system enables volumetric reflection-mode imaging of vasculature and bones in human extremities such as the arm[19]. However, both of these systems' parameters (for example, array dimensions, acoustic frequency and power, and detection sensitivity) are not yet suitable for human-scale imaging in regions such as the adult human abdomen.

In this work, we developed a system that enables UST of the entire human cross-section, resulting in two-dimensional (2D) images of reflectivity, speed of sound and attenuation coefficient profiles. We constructed a custom 512-element circular receiver array combined with a single-element transmitter that rotates around the participant. This geometry enables both reflection- and transmission-mode imaging with improved robustness to acoustic occlusions, while maintaining practicality for in vivo human abdominal imaging compared with planar or hemispherical alternatives. To image deep in the body, we enhance the signal sensitivity by using low-noise parallel preamplifiers directly coupled with the receiver array and by exciting the transmitter with a chirp waveform. Compared with handheld probes, we reduce issues of acoustic shadowing from regions containing bone or air pockets by using full 360° viewing angles. In comparison with MRI and other standard imaging modalities, whole cross-sectional UST is a potential low-cost, safe, fast and convenient tool for screening and monitoring abdominal conditions.

We demonstrate this technique by imaging cross-sections of the abdomen and legs of healthy volunteers, where we clearly observe several organs and key features in reflection-mode images, and we obtain profiles of speed of sound and attenuation coefficient. This approach visualizes abdominal adipose layers, offering a promising modality for mapping adipose thickness distributions without ionising radiation or tissue compression. We also demonstrate a method for localizing biopsy needle tips deep in tissue with respect to internal features. By coupling an acoustic transmitter to a commercial needle and detecting the resulting scattered signals from the needle tip, we obtain 30-frame-per-second images of the needle tip location. Together, these techniques showcase whole cross-sectional UST as a safe and practical modality for a variety of clinical applications.

Results

Whole cross-sectional human imaging

We developed a custom 60-cm-diameter, 512-element circular acoustic receiver array with 1 MHz centre frequency. A 1.5-inch-diameter transducer (Olympus V395) with a custom cylindrical diverging polymethylpentene (TPX) lens is used as a transmitter, and it is mounted on a plastic gear that rotates around the participant using a stepper motor. All receiver channels are preamplified using custom circuit boards within the array (Supplementary Fig. 1), and these signals are digitized in parallel using two data acquisition modules (Photosound Legion) housed in shielded enclosures. The array is mounted on two vertical motor stages to adjust its height in a water immersion tank. The water acts as acoustic coupling between the skin and transducers. An arbitrary function generator (Siglent SDG2042X) connected to a 300-W RF power amplifier (ENI A300) excites the transmitter. The system hardware is shown in Fig. 1a.

To enhance the signal-to-noise ratio (SNR) without exceeding the mechanical index (MI) safety standard, we use a 400-µs chirp signal spanning 0.3–2.0 MHz. We first record the transducer response using only water in the imaging domain, which is then cross-correlated with the target response to recover a pulse-like representation. We show example signals from the receiver array for water and the human abdomen in Fig. 1d,e, showing both backscattered and transmitted signals recorded in parallel. Figure 1f shows pulse-compressed signals obtained through cross-correlation with the water reference. This approach also enables channel calibration using the water scan, where we expect the same received amplitude for channels directly opposite the transmitter.

We demonstrate cross-sectional UST in healthy volunteers. For abdominal imaging, participants sit on a stool in the water immersion tank with their head supported against a cushion to reduce motion and with their arms raised to elevate the ribcage. During a 10-s scan, participants are asked to hold their breath while remaining motionless. Figure 2a shows example reflection-mode images of the abdomen of a 31-year-old female volunteer (participant 1). The images are displayed in inverse greyscale (brighter regions are more anechoic) normalized to the peak pixel amplitude. The outer boundary is extracted using an automated segmentation tool[20]. We performed scans at 1-cm vertical intervals, from approximately the ribcage to the pelvis. The participant was in the immersion tank for approximately 10 min over the entire imaging session. With the same volunteer standing in the immersion tank, we also imaged the thighs (Fig. 2b), where the femur, surrounding muscle groups and adipose boundaries are observed.

We compare our abdominal images with T1-weighted images from 3-T MRI (Siemens Prisma) in Fig. 3. The elevational slices between UST and MRI are aligned using the navel as a reference point. UST visualizes various structures, such as the liver, stomach, kidneys, abdominal aorta, vena cava and vertebral body. We labelled regions using an anatomical atlas and through consultation with a clinical collaborator. Supplementary Video 1 compares the UST and MRI images across all slices. Note that despite the presence of bone and potential air pockets, our geometry enables imaging of regions deep in the body. Owing to our lower acoustic frequency compared with that in typical probe-based ultrasonography, our images primarily correspond to reflections from tissue boundaries rather than scattering within tissues[21].

Acoustic signals transmitted through the body enable reconstruction of speed of sound and attenuation coefficient maps by comparing arrival time and amplitude, respectively, with those from the water-only scan. We show example reconstructions for a 23-year-old female volunteer (participant 2) overlaid on reflection-mode images in Fig. 4c,d. The liver exhibits a higher speed of sound than surrounding organs, consistent with literature values[22], while elevated attenuation is observed in the spine and stomach. Overall, the measured values are in good agreement with literature reports for multiple organs, including the liver (Supplementary Fig. 11). To validate this method, we imaged reference ethanol–water mixtures containing five targets (~3 cm diameter) with speeds of sound ranging from 1,510 to 1,610 m s^{-1}. Our estimates demonstrated less than 3% error (Supplementary Table 4), supporting the potential of this approach for quantitative evaluation of conditions such as liver fibrosis and non-alcoholic fatty liver disease[23]. We show the reconstructed speed of sound and attenuation coefficient for participant 1 in Supplementary Figs. 4 and 5.

Human adipose imaging

Subcutaneous adipose (SA) and preperitoneal adipose (PA) distributions serve as key indicators of metabolic health[24]. SA thickness can be measured with calipers and probe-based ultrasound. Calipers are known to be less accurate for individuals with larger SA thickness, are operator-dependent and have only moderate agreement with estimates from MRI[25]. Probe-based ultrasound, though more accurate and capable of measuring PA thickness than calipers[26], requires extensive operator training and suffers from probe-induced tissue compression[27]. Both methods also require instrument repositioning at each measurement site, making frequent whole-body adipose distribution assessment impractical[28]. We compare our approach with existing methods in Supplementary Table 2.

https://doi.org/10.1038/s41551-026-01660-4

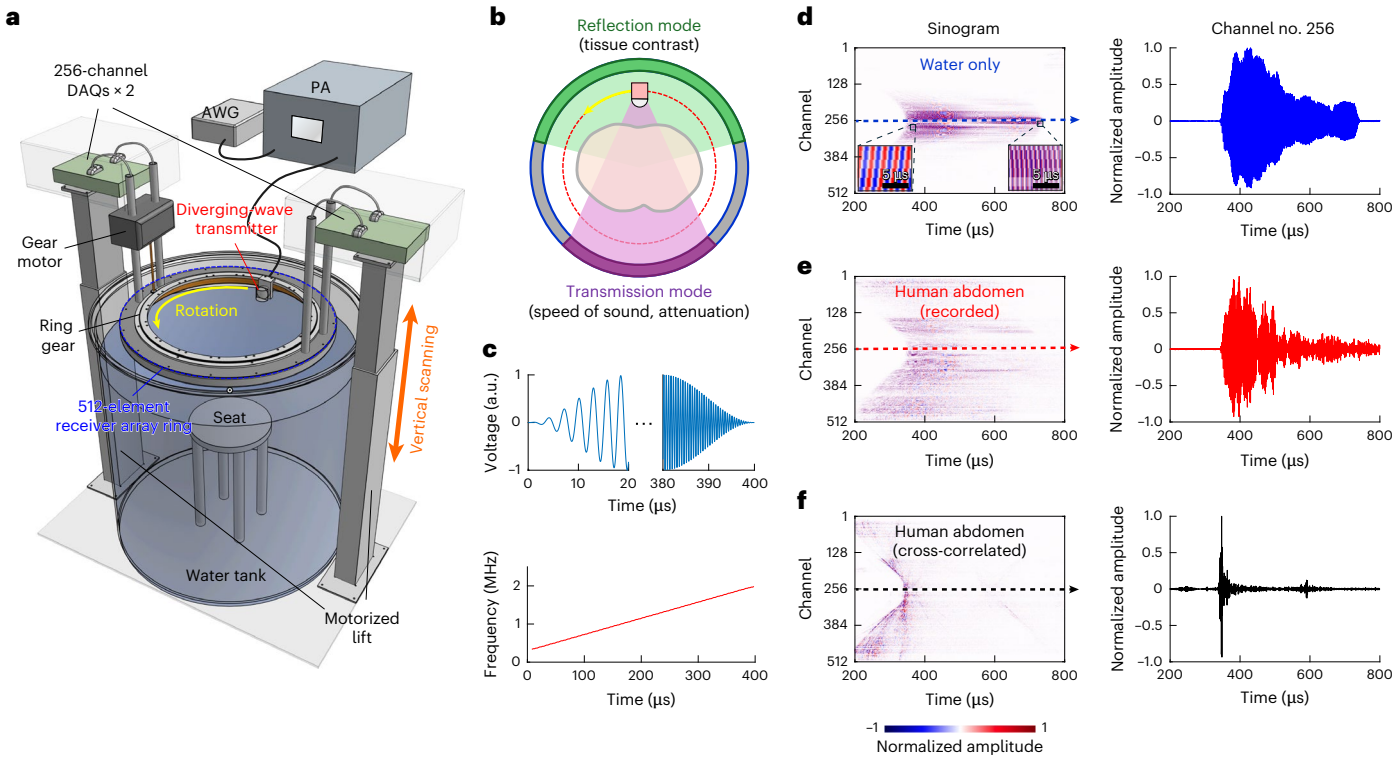

Fig. 1 | UST system for whole cross-sectional human imaging. a, The system diagram. **b**, A schematic diagram of the orbiting single-element transmitter and receiver ring array. During a 10-s scan, the diverging-wave transmitter rotates around the body while all 512 receivers record the backscattered (reflection mode) and transmitted (transmission mode) signals. The coloured sectors on the receiver ring indicate the acoustic aperture window for reflection imaging (green, 160° angular aperture) and transmission imaging (purple, 90° aperture), which provide tissue contrast and quantitative parameters such as speed of sound or attenuation coefficient, respectively. **c**, A chirp excitation waveform. Top: temporal profile of the amplified chirp-encoded waveform coupled to the transmitter, with Hamming window apodization at the beginning and end of the signal. Bottom: instantaneous frequency of the 400-μs chirp signal spanning 0.3–2.0 MHz. **d**–**f**, A demonstration of pulse compression in received time-domain channel data. The left column shows sinograms, while the right column shows a recorded signal profile from channel 256 (dashed line in the sinogram), with the following: a reference recording in water (**d**), where the inset images display the initial and terminal segments of the chirp pulse, highlighting the gradual increase in frequency content; a raw signal recorded from the human abdomen (**e**); and a pulse-compressed signal obtained by cross-correlating **e** with the corresponding water reference (**f**), demonstrating recovery into a sharp profile. AWG, arbitrary waveform generator; DAQs, data acquisition modules; PA, power amplifier.

Cross-sectional UST offers unique advantages for SA assessment by enabling clear visualisation of the adipose layers around the abdominal periphery without mechanical deformation. To validate this approach, we first imaged a phantom consisting of a lard layer of varying known thicknesses, held in place with plastic ribbon over a 4% agar core. We extracted the reflection-mode image amplitude along lines normal to the phantom surface. We estimated the lard layer thickness by determining the distance between the two dominant peaks along this line (Supplementary Fig. 15). Our estimated thicknesses of 1.04 ± 0.02 cm and 2.02 ± 0.05 cm agree well with the true values of 1.00 cm and 2.00 cm, respectively, despite a lower speed of sound in lard (~1,440 m s^{-1} versus ~1,500 m s^{-1} in water).

We compare in vivo adipose regions identified by UST and fat-only T1-weighted MRI in Fig. 5a–d in participant 1. This participant has a body mass index (BMI) of 18.8 kg m^{-2}. Two distinct SA layers are visible: the superficial adipose layer (SAL) and the deep adipose layer (DAL). We extract profiles in the UST and MRI images to estimate the SA thickness along three lines (Fig. 5b–d). We estimate the thickness using the two dominant amplitude peaks for UST and the 50% normalized intensity crossings for MRI. Because the MRI images are acquired with the participant in the supine position, we choose regions that are less susceptible to adipose deformation[28]. The measurements show very close agreement, with differences of less than 1 mm between UST and MRI. Additional profiles are shown in Supplementary Fig. 16. We then imaged a 27-year-old male volunteer (participant 3) with BMI of 25.1 kg m^{-2} and greater SA thickness (Fig. 5e). The anterior side of the abdomen clearly shows the SA and PA regions relative to the skin surface and rectus abdominus muscles. Within the SA, we observe the SAL and DAL, separated by the superficial (or Scarpa's) fascia[29–31]. We show additional images for participant 3 in Supplementary Fig. 6. Because whole cross-sectional UST is fast, safe and more cost-effective than MRI, it shows promise for guiding and assessing weight loss regimes, clinical trials of weight loss drugs or liposuction planning and evaluation[32].

Biopsy needle localization

Next, we demonstrate UST-guided biopsy needle localization. In clinical practice, tissue samples from suspected cancerous regions are collected via needle biopsy, typically guided by ultrasound or X-ray CT imaging[33]. However, probe-based ultrasound localization is generally only used for superficial targets like in the breast, and it requires that the needle is approximately orthogonal to the imaging probe to provide sufficient backscatter to the probe. While manufacturers have developed treatments like scoring or bubble-filled polymer coatings to generate more isotropic scattering and improve the ultrasound visibility[34], these approaches can increase the insertional friction of the needle[35]. Moreover, probe-based localization requires the operator to simultaneously manipulate both the probe and needle, which requires substantial training[36] and becomes particularly challenging in complex tissue regions. Computed tomography (CT) needle guidance, while providing whole-body localization, involves a cumbersome workflow

https://doi.org/10.1038/s41551-026-01660-4

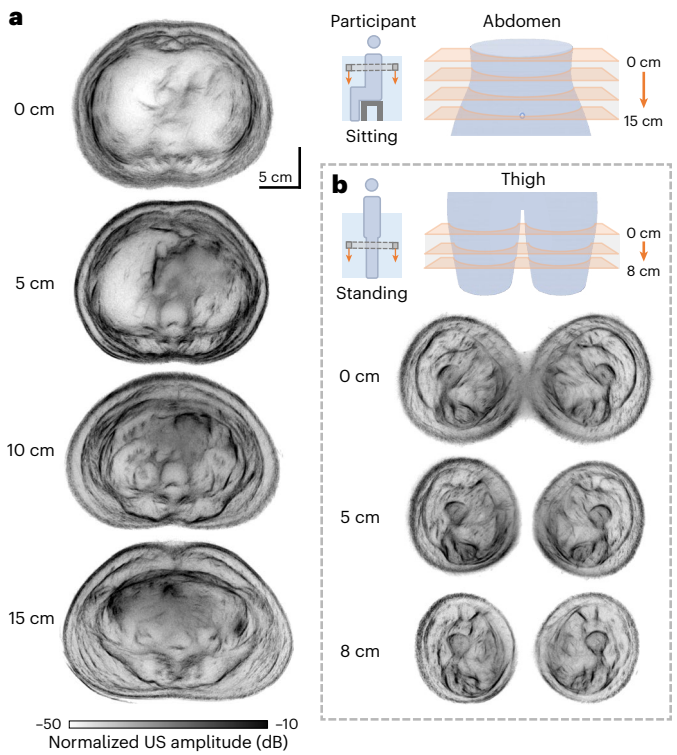

Fig. 2 | Whole cross-sectional UST of a healthy adult female (participant 1). **a**, Serial UST slices of the abdomen spanning from approximately the ribcage to the pelvis, acquired with the participant seated in the water immersion tank. The sequential cross-sections delineate abdominal organs, musculature and adipose distributions. **b**, UST images of the thighs acquired with the participant standing in the tank, demonstrating clear separation of subcutaneous fat and musculoskeletal compartments. The full scanned image sequences are available in Supplementary Fig. 3.

requiring multiple positioning cycles. Each adjustment requires the clinical team to exit and re-enter the scanning room, taking several minutes to complete. This interrupted workflow, combined with a concerning radiation exposure (approximately 10 mSv) (ref. 37), highlights the need for alternative guidance approaches.

Our approach uses a commercial 16-gauge core biopsy needle consisting of a solid stainless-steel core (1.5 mm diameter) that translates within a hollow sleeve. We found that ultrasound signals can be coupled into the unmodified needle using an ultrasonic transducer interfaced with the plastic handle. These signals propagate along the needle as an acoustic waveguide, and they are scattered nearly isotropically at the needle tip (Fig. 6a). To enhance SNR, we employ the same chirp signal used in UST imaging. The scattered signals from the tip are detected with our acoustic array and are cross-correlated with the water chirp response. The propagation time along the needle is calibrated for and remains constant. We expect the dominantly excited mode to be longitudinal with approximately constant phase velocity over our frequency range (Supplementary Fig. 14).

The needle tip location is determined using one-way delay-and-sum beamforming, accounting for the propagation time along the length of the needle. The needle's image response (Fig. 6b) demonstrates a full width at half maximum (FWHM) of ~0.7 mm. This approach enables 30-frame-per-second needle localization over a human-scale FOV. Example video frames (Fig. 6c,d) show the needle response overlaid on a UST reflectivity image of an agarose phantom supported by a steel post. We normalize the needle response images by the same expected maximum value across all video frames. The needle's centre response is automatically determined on the basis of the 5th-order moment of the needle image. The full video is provided in Supplementary Video 2. As seen, the acoustic image quickly and accurately tracks the location of the needle tip with respect to the phantom, even when moving rapidly or inserted into the tissue. To validate this approach in more realistic conditions, we used layered ex vivo porcine tissue (consisting of skin, adipose and muscle) as an anatomical phantom. With the needle oriented approximately horizontally, this approach tracks its position during movement around and into the tissue (Fig. 6e,f). Supplementary Video 2 demonstrates continuous localization of the needle tip throughout the insertion path.

Discussion

We developed a system for whole cross-sectional human ultrasound imaging that advances beyond conventional probe-based ultrasonography in several key ways. Our approach captures complete body cross-sections while simultaneously providing three contrast mechanisms: reflectivity, speed of sound and attenuation coefficient. Conventional short pulses would yield substantially reduced signal after penetrating the entire human body. To improve the SNR, we employ chirped pulses in conjunction with matched filtering, enabling us to achieve higher-quality images. Chirped signals deliver more ultrasound energy while adhering to safety standards. Unlike clinical ultrasonography, which requires extensive operator training to visualize regions of interest, our approach could be largely automated since it requires minimal participant positioning. These advantages could be particularly attractive for applications requiring frequent imaging, and they could help reduce costs compared with other modalities.

Cross-sectional UST offers several potential clinical applications that warrant further study. This technique could enable screening of organs or tissue for indications of inflammation or disease[38]. For instance, liver cirrhosis may be visualized and tracked over time. Aortic aneurysms may also be visualized with UST in patients who are often asymptomatic. The quantitative measurements of speed of sound and attenuation coefficient could serve as diagnostic tools, for instance, to assess changes due to non-alcoholic fatty liver disease[38]. In addition, our speed of sound maps could enhance acoustic focusing in therapeutic applications such as shockwave lithotripsy for kidney or gallbladder stones. Pancreas screening represents an important potential application of our technique, as no dedicated screening tool currently exists for this purpose.

Compared with other emerging techniques, such as low-field MRI[39], whole cross-sectional UST is faster (~10 s per 2D slice) with comparable or finer resolution (~1 mm), and it does not require a shielded room or a magnet-compatible environment. Further, it is more portable, more open and less noisy than MRI. Owing to its magnet-free operation, it can be used for participants with implants that are incompatible with MRI. Together, these features make cross-sectional UST a potential practical tool for clinical needs currently unmet by other modalities. Although our system's resolution does not match clinical CT or MRI, it offers unique advantages for longitudinal monitoring by enabling frequent scans without ionising radiation exposure, large-magnet hazards or lengthy scanning times. The system's efficiency in both cost and time could make it practical to track changes over weeks or months, especially for conditions where broad structural changes are most relevant, such as organ size variation or adipose redistribution. The cost of UST patient care per visit is substantially lower compared with standard MRI, and the shorter visits also provide greater convenience for patients. We provide a comparison of cross-sectional UST with other clinical modalities in Supplementary Table 1.

Our large FOV enables adipose assessment around the entire body. Unlike calipers or probe-based ultrasound, this approach visualizes SA and PA around the entire periphery without mechanical deformation. This could be an appealing tool for liposuction planning and evaluation, weight loss monitoring[40] or pharmaceutical trials for anti-obesity drugs, where MRI and CT are prohibitively costly or harmful. Improved

https://doi.org/10.1038/s41551-026-01660-4

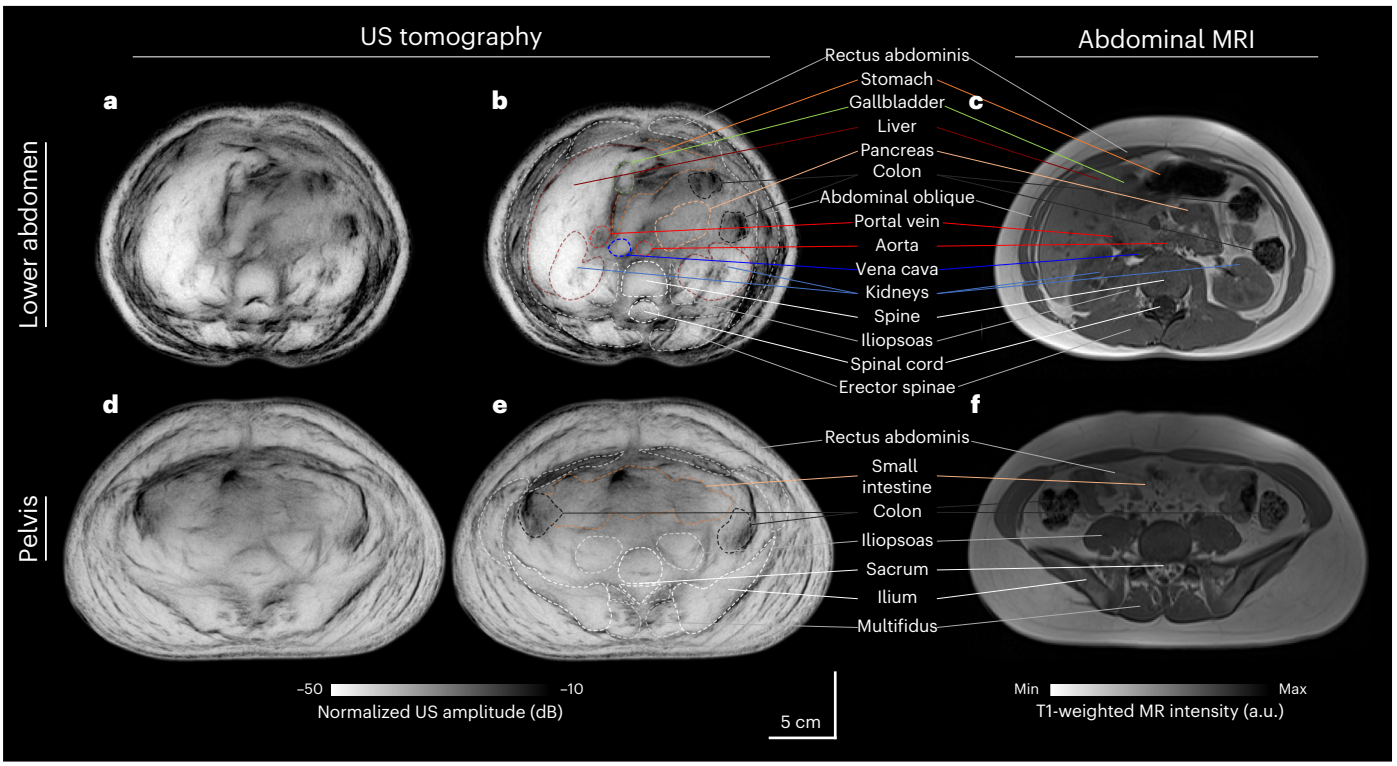

Fig. 3 | Example reflection-mode UST images of a healthy female's abdomen (participant 1) compared with T1-weighted MRI. a, An unlabelled reflection-mode UST image 6 cm inferior to the starting position. **b**, A labelled UST image identifying various organs and structures. **c**, A T1-weighted MRI image of a corresponding region. **d**, An unlabelled UST image 15 cm inferior to the starting position. **e**, A labelled UST image. **f**, An MRI image of a corresponding region.

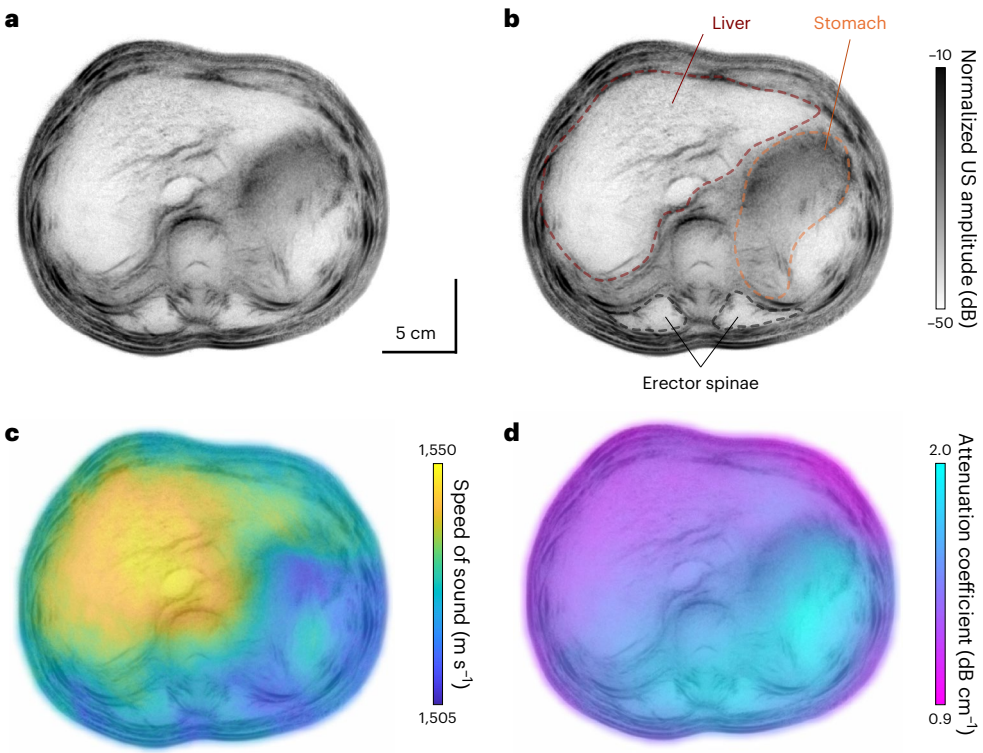

Fig. 4 | Quantitative tissue property mapping from transmission-mode UST in a healthy female (participant 2). a,**b**, A reflection-mode UST image (**a**), with representative organs and anatomical landmarks labelled (**b**) (liver, stomach and erector spinae). **c**, The speed of sound overlaid on **a**, demonstrating distinct acoustic velocities across different tissue compartments. **d**, An attenuation coefficient map overlaid on **a**, highlighting contrast between tissue regions.

https://doi.org/10.1038/s41551-026-01660-4

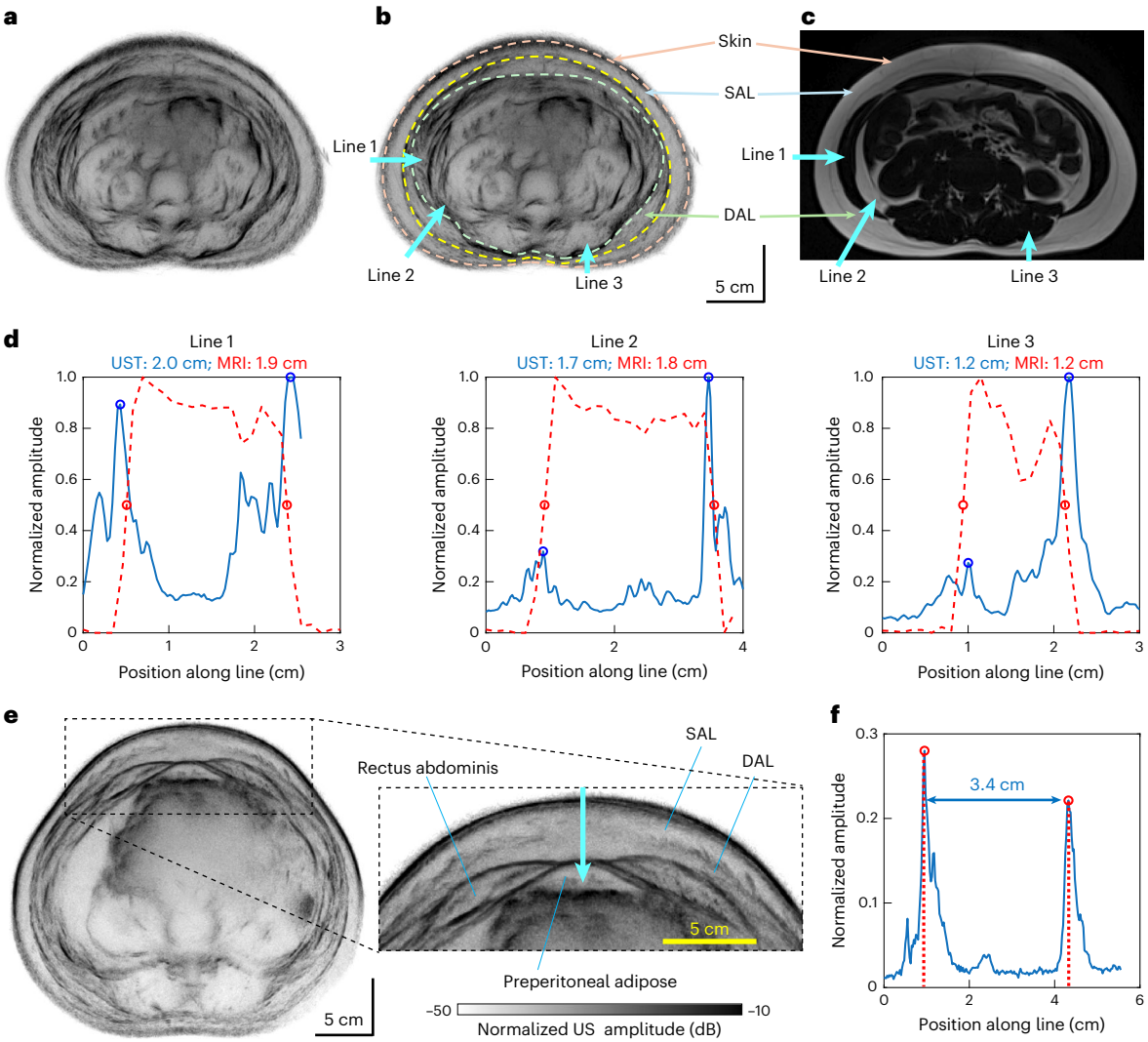

Fig. 5 | Abdominal adipose imaging in healthy volunteers. a, An unlabelled UST image 10 cm inferior to the starting position in a healthy female (participant 1, BMI of 18.8 kg m^{-2}). **b**, A labelled UST image highlighting the differentiation of the skin, SAL and DAL. The cyan arrows show the lines used for the thickness estimation in **d**. **c**, The T1-weighted fat-only MRI reconstruction of a corresponding region. **d**, The extracted line profiles used to estimate adipose thickness with UST (blue) and MRI (red). The circles show the estimated adipose boundaries. **e**, An abdominal UST of a healthy male (participant 3, BMI of 25.1 kg m^{-2}). **f**, An extracted UST line profile.

image quality or contrast may further enable the evaluation of visceral adipose regions. Muscle regions are also observed in our images (for example, abdominal and leg muscles), which may be useful for guiding athletic training. A key advantage of our system is the intuitive nature of the cross-sectional images, which may reduce the amount of trained analysis required compared with conventional ultrasound. While interpretation is currently aided by clinical collaborators, future development of automated analysis pipelines could further enhance usability. In particular, artificial intelligence-based segmentation and organ labelling methods, such as those developed for MRI or CT[39], could provide guidance and annotation for non-expert users. Such advances could facilitate longitudinal screening and broaden the scalability of this technology for use in diverse clinical settings.

Cross-sectional UST shows promise in image-guided needle biopsy, where X-ray imaging is conventionally used. Our human-width FOV enables biopsy needle localization relative to internal features without ionising radiation. Unlike CT guidance, which requires iterative needle positioning and imaging, UST provides real-time feedback during insertion. This technique could also be used for localization during minimally invasive robotic surgery[41], where the needle or tool tracked relative to internal features is particularly valuable during procedures that deform tissues.

Our current 10-s slice acquisition time enables imaging within a single breath hold. Two primary factors limit shorter acquisitions: the mechanical scanning rate of the transmitter and the data acquisition transfer rate, which depends on the repetition rate and acquisition length. We could achieve faster scanning using a slip ring for electrical connection to the transmitter and a more powerful driving motor. Given the ~1-ms round-trip acoustic propagation time within the immersion tank, the repetition rate could potentially increase from our current device limit of 180 Hz to ~1 kHz. While an acoustic array could also be used to transmit and receive signals, this may compromise sensitivity due to electrical switching and reduced chirp signal length and quality. Water immersion could be eliminated through several alternatives: inflatable water bags such as those used in shockwave lithotripsy[42], gel or liquid standoff pads[43], or with skin-coupled conformal acoustic arrays[44]. However, water immersion may be practical for specific applications such as assessing adipose distribution. For example, fitness or wellness centres could conveniently integrate immersion-based scanning where users already swim or bathe. These

https://doi.org/10.1038/s41551-026-01660-4

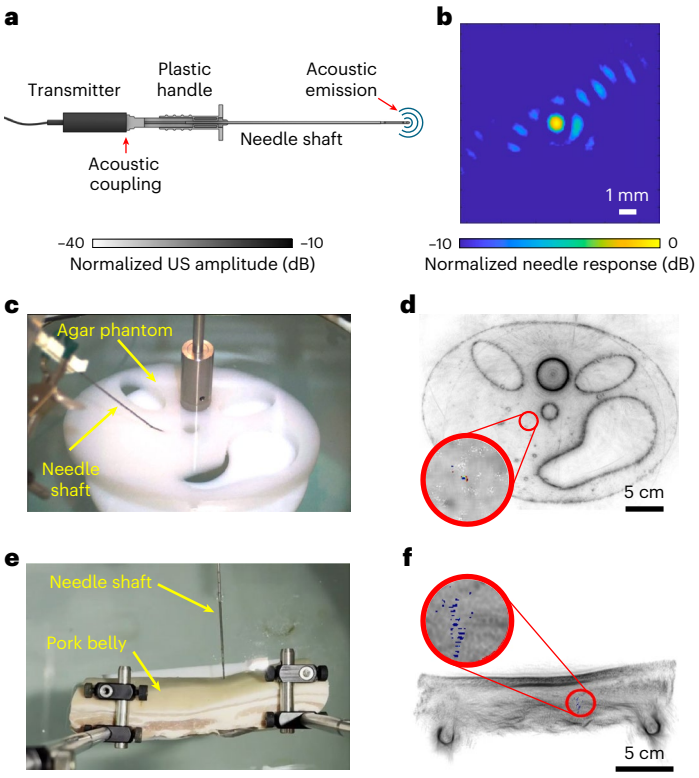

Fig. 6 | UST-guided biopsy needle localization. a, A schematic of the needle configuration. **b**, The acoustic response of the needle tip in water. **c**, A photograph showing the needle inserted into an agar phantom. **d**, The corresponding reconstructed frame overlaid on the reflection-mode UST image, with the red circle marking the automatically detected needle tip as the centroid of the acoustic response. **e**, Needle insertion into ex vivo pork belly tissue. **f**, The reconstructed frame overlaid on the reflection-mode UST image. The full video sequences are provided in Supplementary Video 2.

users might value periodic scans to track changes in adipose and muscle thickness, similar to how dual-energy X-ray absorptiometry is used to monitor body composition[45].

In the future, we also plan to enhance this system with additional laser-induced photoacoustic and microwave/radiowave frequency-induced thermoacoustic contrast. Using the same acoustic receivers, these images would be inherently coregistered with our UST images to overlay optical and microwave/radiowave frequency absorption profiles. We also plan to improve our transmission-mode reconstruction quality using techniques such as full-wave inversion[46], enabling better localization of the speed of sound and attenuation coefficient variations. Additional acoustic elements could also reduce image acquisition time and provide three-dimensional imaging capability.

Methods

System hardware

We developed a custom 512-element, 60-cm-diameter acoustic receiver array with a 1-MHz centre frequency. This geometry is scaled from similar systems for small animal or human breast photoacoustic imaging[47,48]. We use lower acoustic frequencies than typical handheld probes or breast UST systems to enable whole cross-sectional imaging. For instance, the typical acoustic attenuation of ~1 dB cm^{-1} MHz^{-1} results in ~30 dB attenuation across a typical 30-cm-diameter human cross-section at 1 MHz (ref. 21).

All 512 receiver array elements are 1-mm-thick, 3 mm × 10 mm gold-coated piezoelectric polymer (PVDF-TrFE, PolyK Technologies LLC). We selected PVDF-TrFE for its broad bandwidth and ease of manufacturing. Its acoustic impedance (~4.2 MRayl) is also more closely matched to casting epoxy backings (~3.5 MRayl) and water (~1.5 MRayl) than other piezoelectric materials. Each element is capacitively coupled to copper-clad polyimide electrodes by bonding with high-strength epoxy. A continuous copper-clad polyimide electrode is used for ground reference. The electrodes are then directly connected to parallel preamplifiers implemented on custom annular printed circuit boards. The preamplifiers provide 15 dB of voltage gain with 100 kΩ input impedance. Further construction details are shown in Supplementary Figs. 1 and 2.

We machined a 60-cm-diameter plastic disc and used it as a mould for the inner surface of the array. The elements and preamplifiers are housed in a stainless-steel shielded enclosure, with coaxial cables for each element connected through stainless steel holding tubes. Casting epoxy serves as the backing material for each element, and we incorporate an angled back panel to reduce acoustic reverberation. All channels are low-pass filtered (f_c = 2 MHz) and digitized (Photosound Legion) in parallel at 5 million samples per second using 20 dB of additional gain. The digitizers are controlled and transfer data through USB over optical fibre to reduce interference. The preamplifiers are powered by rechargeable lithium-polymer batteries, which feature a d.c. voltage regulator to minimize electrical noise. To account for geometrical error during manufacturing, the technique described in ref. 49 is used to calibrate each element's position.

The gear rotation is driven by a stepper motor. An optical homing switch is used to ensure a consistent initial rotation angle. Plastic hooks are mounted on the gear to hold the transmitter cable on the gear surface during rotation (Supplementary Video 3).

Acquisition parameters

To enhance the SNR while being limited by the MI, a linear chirp signal versus time (t) is used with a time-varying frequency $f(t) = f_r t + f_0$, where $f_r = (f_1 - f_0)/T$ is the linear chirp rate, f_0 = 0.3 MHz is the lower frequency, f_1 = 2.0 MHz is the upper frequency and T = 400 µs is the chirp duration. The transmitted frequencies are limited by the bandwidths of the transmitter and receivers. We used a maximal pulse duration given our maximal acquisition time of 800 µs, enabling recovery of the round-trip reflected signals over the entire FOV. The resulting transmitted chirp signal is

$$x(t) = \sin\left[2\pi\left(\frac{f_r}{2}t^2 + f_0 t\right)\right]. \quad (1)$$

Compared with a pulse with similar peak pressure, this results in an expected SNR gain of $\sim\sqrt{T \times B}$, where $B = f_1 - f_0$ is the acoustic bandwidth[50]. In addition to the target, we also perform a scan with only water in the imaging domain, resulting in recorded signals $x_{w,i}(t)$ for each receiver element i. This provides the response of each transducer to the chirp, which is then cross-correlated with the target's chirp response $x_{c,i}(t)$. The pulse response for the target signals $\chi_{s,i}(t)$ is then recovered for each element i as

$$\chi_{s,i}(t) = \frac{x_{w,i}(t) \star x_{c,i}(t)}{\max\left[x_{w,i}(t) \star x_{w,i}(t)\right]}, \quad (2)$$

where ⋆ denotes cross-correlation. We normalize by the maximum of the autocorrelation of $x_{w,i}(t)$ to account for sensitivity variation in the receiver elements. The transmitter operates with a pulse repetition rate of 180 Hz. With the gear rotation time of 10 s, this results in 1800 transmitted pulses over a full circular scan around the target.

Reflection-mode reconstruction algorithm

We employ a 2D delay-and-sum algorithm for reflection-mode ultrasound reconstruction. We first cross-correlate each channel's recorded signal with its direct transmission water-only response to obtain a pulse-like

representation. We then band-pass filter the cross-correlated signals within 0.3–2.0 MHz and normalize them on the basis of the water-only autocorrelation. We use the Hilbert transform to obtain complex representations of the signals, which are used for reconstruction. Then, for each transmitter position, we determine the time delay between the transmitter focal point and each pixel for a given background speed of sound. We mathematically correct for the angle-dependent focal point with the acoustic lens, as shown in Supplementary Fig. 13. Next, we calculate the delay time from each pixel to each receiver position. We use the 256 receiver channels on the side of the transmitter to limit reconstruction to backscattered signals. For each transmitter position, complex pixel values are found from the sum of the cross-correlated received signals at the total round-trip delay time.

After forming the angle-stacked complex image for each transmitter position, we improve image quality with coherent-subset scaling. The transmitter positions are partitioned into overlapping subsets of $M = 80$ consecutive angles, advanced by $M/2$ so that each new subset shares 50% of its angles with the previous one. Within every subset, we apply a Hann angular apodisation, coherently sum the complex data and take the magnitude to generate an envelope image for that subset. Finally, we incoherently average the envelopes from all subsets to produce a compounded amplitude image. This procedure preserves coherent information within each narrow angular window while suppressing speckle through incoherent averaging across windows, resulting in a cleaner, higher-contrast reflection image.

We implemented this algorithm using CUDA kernel from MATLAB, computed using a NVIDIA GeForce RTX 3070 graphics processing unit. Reconstruction was performed over a 512 mm × 512 mm grid with 0.125 mm × 0.125 mm pixel size, consisting of 4,096 × 4,096 pixels. For each slice, the required computational time was approximately 12 min. We expect this could be greatly shortened with more capable graphics processing units. To visualize the images, we first used a 2D Wiener filter with a 4-pixel neighbourhood size. We then normalized the images to their maximum amplitude and displayed them on a logarithmic scale. Background segmentation was carried out using an automated segmentation tool[20].

Image quality

We assessed our in-plane resolution using a thin (<0.1 mm) metallic wire. The reconstructed image and axis profiles are provided in Supplementary Fig. 8. We find an in-plane FWHM of approximately 0.9 mm. To determine our elevational resolution, we imaged a thin brass disc positioned such that its edges were at the centre and outer boundary of our typical FOV. The height of the disc was scanned, and a UST image was obtained at 2.5-mm increments. An elevational FWHM of 15 mm and 25 mm was found for the centre and edge of the FOV, respectively. Neither the transmitter nor the receivers are focused in the elevational direction, but their larger dimensions in this direction reduce their acceptance angles.

Human imaging protocol

Five volunteers (three female and two male participants) consented to be imaged using this system. This imaging procedure was approved by the Caltech Institutional Review Board (protocol IR21-1099). Before human imaging, we used a calibrated hydrophone (Onda HGL-0085) positioned immediately in front of the transmitter to evaluate the safety of our system. We used an MI of less than 0.2 over the entire chirp bandwidth, whereas the limit set by the US Food and Drug Administration (FDA) is 1.9 (ref. 51). We evaluated the spatial peak temporal average intensity (I_{SPTA}) as 24 mW cm^{-2}, whereas the FDA limit is 720 mW cm^{-2}. We calculated the thermal index from the empirical formula as listed in ref. 52 to be 0.65, which is also much lower than the FDA limit of 6.0 for diagnostic ultrasound devices.

Before imaging, we filled the water immersion tank with warm (~30 °C) tap water using rubber tubing. We provided a private room for volunteers to change into a swimsuit and to dry using a towel and space heater after the imaging session. Volunteers entered the tank using an external ladder with handrails and anti-slip coatings (Supplementary Fig. 18). After volunteers entered the water tank, we asked them to use their hands to wipe away air bubbles that may have accumulated on their abdomens. An emergency off button was accessible to the volunteers during scanning, shutting electrical power to all system devices. All electrical devices were powered through a ground-fault circuit interrupter in case of water exposure. The operators ensured volunteer comfort verbally and visually. The volunteers remained seated on an immersed stool during image acquisition with their shoulders resting on a backrest to reduce motion. We performed these human experiments in a dedicated imaging room. Written informed consent was obtained from participants in accordance with our insitutional review board protocol. Volunteers were compensated US$100.

Reporting summary

Further information on research design is available in the Nature Portfolio Reporting Summary linked to this Article.

Data availability

The data that support the findings of this study are provided within the article and its Supplementary Information. A representative ultrasound dataset is available via Figshare at https://doi.org/10.6084/m9.figshare.31043818.v2 (ref. 53). Owing to the large size of the full raw ultrasound datasets (>100 GB), these data are not publicly deposited but are available from the corresponding author upon reasonable request.

Code availability

The reconstruction algorithm and data processing methods can be found in the article. The reconstruction code is not publicly available because it is proprietary and may be used in licensed technologies.

References

1. Holmes, J. H. & Howry, D. H. Ultrasonic diagnosis of abdominal disease. *Am. J. Dig. Dis.* **8**, 12–32 (1963).
2. Howry, D. H. & Bliss, W. R. Ultrasonic visualization of soft tissue structures of the body. *J. Lab. Clin. Med.* **40**, 579–592 (1952).
3. Goldberg, B. B., Gramiak, R. & Freimanis, A. K. Early history of diagnostic ultrasound: the role of American radiologists. *AJR Am. J. Roentgenol.* **160**, 189–194 (1993).
4. Holm, H. H. & Mortensen, T. Ultrasonic scanning in diagnosis of abdominal disease. *Acta Chir. Scand.* **134**, 333–341 (1968).
5. Howry, D. H., Holmes, J. H., Cushman, C. R. & Posakony, G. J. Ultrasonic visualization of living organs and tissues; with observations on some disease processes. *Geriatrics* **10**, 123–128 (1955).
6. Holm, H. H. Ultrasonic scanning in the diagnosis of space-occupying lesions of the upper abdomen. *Br. J. Radiol.* **44**, 24–36 (1971).
7. Donald, I., Macvicar, J. & Brown, T. G. Investigation of abdominal masses by pulsed ultrasound. *Lancet* **1**, 1188–1195 (1958).
8. Pinto, J., Azevedo, R., Pereira, E. & Caldeira, A. Ultrasonography in gastroenterology: the need for training. *GE Port. J. Gastroenterol.* **25**, 308–316 (2018).
9. Noorkoiv, M., Nosaka, K. & Blazevich, A. J. Assessment of quadriceps muscle cross-sectional area by ultrasound extended-field-of-view imaging. *Eur. J. Appl. Physiol.* **109**, 631–639 (2010).
10. Weng, L. et al. US extended-field-of-view imaging technology. *Radiology* **203**, 877–880 (1997).
11. Sauerbrei, E. E. Extended field-of-view sonography: utility in clinical practice. *J. Ultrasound Med.* **18**, 335–341 (1999).

12. Kim, S. H., Choi, B. I., Kim, K. W., Lee, K. H. & Han, J. K. Extended field-of-view sonography. *J. Ultrasound Med.* **22**, 385–394 (2003).
13. Wiskin, J., Borup, D. T., Johnson, S. A. & Berggren, M. Non-linear inverse scattering: high resolution quantitative breast tissue tomography. *J. Acoust. Soc. Am.* **131**, 3802–3813 (2012).
14. Huang, L. et al. Breast ultrasound tomography with two parallel transducer arrays. In *Medical Imaging 2016: Physics of Medical Imaging* (Kontos, D. et al.) 98–109 (SPIE, 2016).
15. Zhang, Y. & Wang, L. Video-rate ring-array ultrasound and photoacoustic tomography. *IEEE Trans. Med. Imaging* **39**, 4369–4375 (2020).
16. Duric, N. et al. Clinical breast imaging with ultrasound tomography: a description of the SoftVue system. *J. Acoust. Soc. Am.* **135**, 2155 (2014).
17. Wiskin, J. et al. Full wave 3D inverse scattering transmission ultrasound tomography: breast and whole body imaging. In *2019 IEEE International Ultrasonics Symposium (IUS)* 951–958 (IEEE, 2019).
18. Wiskin, J. et al. Whole-body imaging using low frequency transmission ultrasound. *Acad. Radiol.* https://doi.org/10.1016/j.acra.2023.01.018 (2023).
19. Park, E.-Y. et al. Fast volumetric ultrasound facilitates high-resolution 3D mapping of tissue compartments. *Sci. Adv.* **9**, eadg8176 (2023).
20. Kirillov, A. et al. Segment anything. In *Proc. IEEE/CVF International Conference on Computer Vision* 4015–4026 (IEEE, 2023).
21. Szabo, T. L. *Diagnostic Ultrasound Imaging: Inside Out* (Academic Press, 2004).
22. Tissue Properties Database V4.2. *IT'IS Foundation* https://doi.org/10.13099/VIP21000-04-2 (2024).
23. Ballestri, S., Romagnoli, D., Nascimbeni, F., Francica, G. & Lonardo, A. Role of ultrasound in the diagnosis and treatment of nonalcoholic fatty liver disease and its complications. *Expert Rev. Gastroenterol. Hepatol.* **9**, 603–627 (2015).
24. Lee, M.-J., Wu, Y. & Fried, S. K. Adipose tissue heterogeneity: implication of depot differences in adipose tissue for obesity complications. *Mol. Aspects Med.* **34**, 1–11 (2013).
25. Kuczmarski, R. J., Fanelli, M. T. & Koch, G. G. Ultrasonic assessment of body composition in obese adults: overcoming the limitations of the skinfold caliper. *Am. J. Clin. Nutr.* **45**, 717–724 (1987).
26. Liu, K. H. et al. Sonographic measurement of mesenteric fat thickness is a good correlate with cardiovascular risk factors: comparison with subcutaneous and preperitoneal fat thickness, magnetic resonance imaging and anthropometric indexes. *Int.J.Obes.* **27**, 10 (2003).
27. Anvery, N. et al. Utility of high-resolution ultrasound in measuring subcutaneous fat thickness. *Lasers Surg. Med.* **54**, 1189–1197 (2022).
28. Hoffmann, J. et al. Measurement of subcutaneous fat tissue: reliability and comparison of caliper and ultrasound via systematic body mapping. *Sci. Rep.* **12**, 1 (2022).
29. Harley, O. J. H. & Pickford, M. A. CT analysis of fat distribution superficial and deep to the Scarpa's fascial layer in the mid and lower abdomen. *J. Plast. Reconstr. Aesthet. Surg.* **66**, 525–530 (2013).
30. Abu-Hijleh, M. F., Roshier, A. L., Al-Shboul, Q., Dharap, A. S. & Harris, P. F. The membranous layer of superficial fascia: evidence for its widespread distribution in the body. *Surg. Radiol. Anat.* **28**, 606–619 (2006).
31. Lancerotto, L. et al. Layers of the abdominal wall: anatomical investigation of subcutaneous tissue and superficial fascia. *Surg. Radiol. Anat.* **33**, 835–842 (2011).
32. Graf, R. et al. Ultrasound-assisted liposuction: an analysis of 348 cases. *Aesthetic Plast.Surg.* **27**, 146–153 (2003).
33. Sainani, N. I. et al. The challenging image-guided abdominal mass biopsy: established and emerging techniques 'if you can see it, you can biopsy it'. *Abdom. Imaging* **38**, 672–696 (2013).
34. Culp, W. C. et al. Relative ultrasonographic echogenicity of standard, dimpled, and polymeric-coated needles. *J. Vasc. Interv. Radiol.* **11**, 351–358 (2000).
35. Li, W., Wang, Y., Nteziyaremye, V., Yamaguchi, H. & Shih, A. J. Measurement of the friction force inside the needle in biopsy. *J. Manuf. Sci. Eng.* **138**, 031003 (2015).
36. Fulton, N., Buethe, J., Gollamudi, J. & Robbin, M. Simulation-based training may improve resident skill in ultrasound-guided biopsy. *Am. J. Roentgenol.* **207**, 1329–1333 (2016).
37. Guberina, N. et al. Radiation exposure during CT-guided biopsies: recent CT machines provide markedly lower doses. *Eur. Radiol.* **28**, 3929–3935 (2018).
38. Allocca, M., Kucharzik, T. & Rubin, D. T. Intestinal ultrasound in the assessment and management of inflammatory bowel disease: is it ready for standard practice? *Gastroenterology* **164**, 851–855 (2023).
39. Barat, M. et al. CT and MRI of abdominal cancers: current trends and perspectives in the era of radiomics and artificial intelligence. *Jpn. J. Radiol.* **42**, 246–260 (2024).
40. Rubino F. et al. Definition and diagnostic criteria of clinical obesity. *Lancet Diabetes Endocrinol.* https://doi.org/10.1016/S2213-8587(24)00316-4 (2025).
41. Siepel, F. J. et al. Needle and biopsy robots: a review. *Curr. Robot. Rep.* **2**, 73–84 (2021).
42. Pfister, R. C., Papanicolaou, N. & Yoder, I. C. Urinary extracorporeal shock wave lithotripsy: equipment, techniques, and overview. *Urol. Radiol.* **10**, 39–45 (1988).
43. Paverd, C., Martin, A., Rominger, M. & Ruby, L. Assessment of ultrasound image quality in a reference phantom using gel and liquid standoff pads. *WFUMB Ultrasound Open* **2**, 100051 (2024).
44. Wang, C. et al. Bioadhesive ultrasound for long-term continuous imaging of diverse organs. *Science* **377**, 517–523 (2022).
45. Shepherd, J. A., Ng, B. K., Sommer, M. J. & Heymsfield, S. B. Body composition by DXA. *Bone* **104**, 101–105 (2017).
46. Cueto, C. et al. Stride: a flexible software platform for high-performance ultrasound computed tomography. *Comput. Methods Programs Biomed.* **221**, 106855 (2022).
47. Li, L. et al. Single-impulse panoramic photoacoustic computed tomography of small-animal whole-body dynamics at high spatiotemporal resolution. *Nat. Biomed. Eng.* **1**, 0071 (2017).
48. Lin, L. et al. Single-breath-hold photoacoustic computed tomography of the breast. *Nat. Commun.* **9**, 2352 (2018).
49. Sastry, K. et al. A method for the geometric calibration of ultrasound transducer arrays with arbitrary geometries. *Photoacoustics* **32**, 100520 (2023).
50. O'Donnell, M. Coded excitation system for improving the penetration of real-time phased-array imaging systems. *IEEE Trans. Ultrason. Ferroelectr. Freq. Control* **39**, 341–351 (1992).
51. Barnett, S. B. et al. International recommendations and guidelines for the safe use of diagnostic ultrasound in medicine. *Ultrasound Med. Biol.* **26**, 355–366 (2000).
52. Duck, F. A. The meaning of thermal index (TI) and mechanical index (MI) values. *BMUS Bull.* **5**, 36–40 (1997).
53. Garrett, D. et al. Human abdominal ultrasound tomography example dataset. *figshare* https://doi.org/10.6084/m9.figshare.31043818.v2 (2026).

Acknowledgements
This work was supported in part by the National Institutes of Health under grant R35 CA220436 (Outstanding Investigator Award); by grant 2024-337784 from the Chan Zuckerberg Initiative DAF, an advised fund of the Silicon Valley Community Foundation; and by the National Research Foundation of Korea grants 2020R1A6A1A03047902 from the Ministry of Education and RS-2024-00335346 from the Ministry of Science and ICT. The funders had no role in study design, data collection and analysis, decision to publish or preparation of the manuscript.

Author contributions
D.C.G., K.M. and L.V.W. conceived of the project. D.C.G., J.X., G.K. and K.M. designed and constructed the system. D.C.G., J.X. and D.O. performed the experiments. D.C.G., J.X., D.O. and Y.A. performed the image reconstruction. D.C.G., J.X., D.O., Y.A., W.W.T. and L.V.W. analysed the data. D.C.G., J.X., D.O., Y.A. and L.V.W. wrote the paper. All authors reviewed and approved the final paper.

Competing interests
L.V.W. has a financial interest in Microphotoacoustics, Inc., CalPACT, LLC, and Union Photoacoustic Technologies, Ltd., which did not support this work. D.C.G., J.X., G.K. and L.V.W. have a provisional patent application titled 'Thermoacoustic and ultrasound tomography', US Patent Application 18/336,863, through the California Institute of Technology, Pasadena, CA, USA. The other authors declare no competing interests.

Additional information
Supplementary information The online version contains supplementary material available at https://doi.org/10.1038/s41551-026-01660-4.

Correspondence and requests for materials should be addressed to Lihong V. Wang.

Peer review information *Nature Biomedical Engineering* thanks the anonymous reviewer(s) for their contribution to the peer review of this work.

nature portfolio

Corresponding author(s): Lihong V. Wang

Last updated by author(s): Jan 08, 2026

Reporting Summary

Nature Portfolio wishes to improve the reproducibility of the work that we publish. This form provides structure for consistency and transparency in reporting. For further information on Nature Portfolio policies, see our Editorial Policies and the Editorial Policy Checklist.

Statistics

For all statistical analyses, confirm that the following items are present in the figure legend, table legend, main text, or Methods section.

n/a	Confirmed	
☐	☒	The exact sample size (*n*) for each experimental group/condition, given as a discrete number and unit of measurement
☐	☒	A statement on whether measurements were taken from distinct samples or whether the same sample was measured repeatedly
☒	☐	The statistical test(s) used AND whether they are one- or two-sided *Only common tests should be described solely by name; describe more complex techniques in the Methods section.*
☒	☐	A description of all covariates tested
☒	☐	A description of any assumptions or corrections, such as tests of normality and adjustment for multiple comparisons
☐	☒	A full description of the statistical parameters including central tendency (e.g. means) or other basic estimates (e.g. regression coefficient) AND variation (e.g. standard deviation) or associated estimates of uncertainty (e.g. confidence intervals)
☒	☐	For null hypothesis testing, the test statistic (e.g. *F*, *t*, *r*) with confidence intervals, effect sizes, degrees of freedom and *P* value noted *Give P values as exact values whenever suitable.*
☒	☐	For Bayesian analysis, information on the choice of priors and Markov chain Monte Carlo settings
☒	☐	For hierarchical and complex designs, identification of the appropriate level for tests and full reporting of outcomes
☒	☐	Estimates of effect sizes (e.g. Cohen's *d*, Pearson's *r*), indicating how they were calculated

Our web collection on statistics for biologists contains articles on many of the points above.

Software and code

Policy information about availability of computer code

Data collection	MATLAB 2020b - 2025a (MathWorks) was used for data collection using custom codes.
Data analysis	MATLAB 2020b - 2025a (MathWorks) was used for data analysis using custom codes. The reconstruction algorithm and data processing methods are described in detail in the Methods.

For manuscripts utilizing custom algorithms or software that are central to the research but not yet described in published literature, software must be made available to editors and reviewers. We strongly encourage code deposition in a community repository (e.g. GitHub). See the Nature Portfolio guidelines for submitting code & software for further information.

Data

Policy information about availability of data

All manuscripts must include a data availability statement. This statement should provide the following information, where applicable:

- Accession codes, unique identifiers, or web links for publicly available datasets
- A description of any restrictions on data availability
- For clinical datasets or third party data, please ensure that the statement adheres to our policy

The data that support the findings of this study are provided within the paper and its Supplementary materials. A representative ultrasound dataset has been deposited in Figshare at https://doi.org/10.6084/m9.figshare.31043818.v2. Due to the large size of the full raw ultrasound datasets (>100 GB), these data are not publicly deposited but are available from the corresponding author upon reasonable request.

Research involving human participants, their data, or biological material

Policy information about studies with human participants or human data. See also policy information about sex, gender (identity/presentation), and sexual orientation and race, ethnicity and racism.

Reporting on sex and gender	Participants were recruited independently of sex or gender. We imaged two male and three female participants.
Reporting on race, ethnicity, or other socially relevant groupings	Race, ethnicity and other social groupings were not considered with regards to the analysis and conclusions of this study.
Population characteristics	All recruited participants were healthy.
Recruitment	Participants were recruited using flyers posted on campus. Interested participants contacted the study coordinators.
Ethics oversight	The study was approved by the Institutional Review Board of the California Institute of Technology.

Note that full information on the approval of the study protocol must also be provided in the manuscript.

Field-specific reporting

Please select the one below that is the best fit for your research. If you are not sure, read the appropriate sections before making your selection.

☒ Life sciences ☐ Behavioural & social sciences ☐ Ecological, evolutionary & environmental sciences

For a reference copy of the document with all sections, see nature.com/documents/nr-reporting-summary-flat.pdf

Life sciences study design

All studies must disclose on these points even when the disclosure is negative.

Sample size	The scope of this work was technology development. We imaged five participants.
Data exclusions	No imaging data were excluded.
Replication	Most participants were imaged during a single session. Two participants were imaged in two sessions after we improved the system hardware. Replications/improvements in image quality were observed.
Randomization	Participants were not randomized. Since this was a pilot study on a new modality, no statistical analysis was performed using participant groupings.
Blinding	Blinding was not possible due to the study authors performing the experiments with a small number of participants. This, however, does not impact our study results.

Reporting for specific materials, systems and methods

We require information from authors about some types of materials, experimental systems and methods used in many studies. Here, indicate whether each material, system or method listed is relevant to your study. If you are not sure if a list item applies to your research, read the appropriate section before selecting a response.

Materials & experimental systems

n/a	Involved in the study
☒	☐ Antibodies
☒	☐ Eukaryotic cell lines
☒	☐ Palaeontology and archaeology
☒	☐ Animals and other organisms
☒	☐ Clinical data
☒	☐ Dual use research of concern
☒	☐ Plants

Methods

n/a	Involved in the study
☒	☐ ChIP-seq
☒	☐ Flow cytometry
☒	☐ MRI-based neuroimaging

Plants

Seed stocks

Report on the source of all seed stocks or other plant material used. If applicable, state the seed stock centre and catalogue number. If plant specimens were collected from the field, describe the collection location, date and sampling procedures.

Novel plant genotypes

Describe the methods by which all novel plant genotypes were produced. This includes those generated by transgenic approaches, gene editing, chemical/radiation-based mutagenesis and hybridization. For transgenic lines, describe the transformation method, the number of independent lines analyzed and the generation upon which experiments were performed. For gene-edited lines, describe the editor used, the endogenous sequence targeted for editing, the targeting guide RNA sequence (if applicable) and how the editor was applied.

Authentication

Describe any authentication procedures for each seed stock used or novel genotype generated. Describe any experiments used to assess the effect of a mutation and, where applicable, how potential secondary effects (e.g. second site T-DNA insertions, mosiacism, off-target gene editing) were examined.